OPEN ACCESS
JOURNAL OF ADVANCED DIELECTRICS
Vol. 13, No. 1 (2023) 2242006 (7 pages)

DOI: 10.1142/S2010135X22420061

Energy storage properties in Nd-doped $AgNbTaO_3$ lead-free antiferroelectric ceramics with Nb-site vacancies

Zhilun Lu[*,§], Dongyang Sun[*], Ge Wang[†], Jianwei Zhao[‡], Bin Zhang[‡], Dawei Wang[‡] and Islam Shyha[*]

[*]*School of Computing, Engineering and The Built Environment*
Edinburgh Napier University, Edinburgh EH10 5DT, UK

[†]*Department of Materials, University of Manchester, Manchester S13 9PL, UK*

[‡]*Shenzhen Institute of Advanced Electronic Materials*
Shenzhen Institute of Advanced Technology
Chinese Academy of Sciences, Shenzhen 518055, P. R. China

[§]z.lu@napier.ac.uk

Received 25 September 2022; Revised 19 October 2022; Accepted 28 October 2022; Published 3 December 2022

It is crucial to discover lead-free materials with ultrahigh recoverable energy density (W_{rec}) that can be employed in future pulse power capacitors. In this work, a high W_{rec} of 4.51 J/cm^3 was successfully obtained in lead-free Nd-doped $AgNb_{0.8}Ta_{0.2}O_3$ antiferroelectric ceramics at an applied electric field of 290 kV/cm. It is discovered that Nd doping paired with Nb-site vacancies could stabilize the antiferroelectric phase by lowering the temperatures of the M1–M2 and M2–M3 phase transitions, which leads to higher energy storage efficiency. Furthermore, Nd and Ta co-doping will contribute to the electrical homogeneity and low electrical conductivity, resulting in large breakdown strengths. Aliovalent doping in Ag-site with Nb-site vacancies serves as a novel strategy for the construction of $AgNbO_3$-based ceramics with excellent energy storage performance.

Keywords: $AgNbO_3$-based ceramics; antiferroelectric; energy storage.

1. Introduction

In advanced pulse power systems, dielectric capacitors with high-power density and rapid charge–discharge rates play a crucial role. Currently, their applications are limited by poor energy density in comparison to batteries and electrochemical capacitors.[1–9] Therefore, dielectric capacitors with enhanced energy storage properties are desperately needed to meet the pressing demand for miniaturization and integration of energy storage devices. The recoverable energy density of ceramic capacitors (W_{rec}) can be calculated by the following equation[10–12]:

$$W_{rec} = \int_{P_r}^{P_{max}} EdP, \tag{1}$$

where P_{max} and P_r are the maximum polarization and the remanent polarization under an applied electric field (E), respectively. Generally, the breakdown strength corresponds to the maximum applied electric field (E_b). When subjected to an electric field, antiferroelectrics can offer a near-zero P_r and a high P_{max}, thus making them promising candidates for achieving high W_{rec}.

Extensive research has been conducted on lead-based antiferroelectrics over the last decade due to their remarkable energy storage properties, but their toxicity drives an environmental and commercial need for lead-free equivalents.[13–15] As alternatives to lead-based materials, $AgNbO_3$ antiferroelectrics exhibit superior energy storage properties and are well-suited for use as dielectric capacitors.[16,17] Recent studies on $AgNbO_3$-based lead-free antiferroelectrics are generally based on the following four strategies: (i) Doping with a small amount of MnO_2 or WO_3 by weight percentage is advantageous for lowering leakage current and grain size, hence contributing to the enhancement of E_b.[18,19] (ii) Various types of dopants, including Ba, Sr, Ca, Bi, La, Sm, Gd, etc., have been used to dope the Ag site with ions of greater valence than Ag.[20–30] iii) Ta is presently the sole substance utilized for doping at Nb site. Reportedly, Ta doping is quite efficient for boosting E_b.[31–33] (iv) Co-doping at Ag and Nb sites, including Sm/Nd and Ta co-doping, has been reported.[24,34] Recent research indicates that the majority of dopants may reduce the grain size of $AgNbO_3$-based ceramics, hence increasing E_b. Among these doped $AgNbO_3$-based ceramics, La-, Gd- and Sm-doped ceramics obtained high W_{rec} of 4.4, 4.5 and 5.2 J cm^{-3},[21,27,35] while the W_{rec} of Ta-doped ceramics are 4.2 and 6.3 J cm^{-3},[31,33] respectively. Literature suggests that ions with a smaller radius than Ag^+ plus A-site vacancies may reduce the tolerance factor, and Ta doping may decrease the

§Corresponding author.

polarizability of the cation at Nb site, both of which enhance the stability of the antiferroelectric phase.

However, the influence of a combination of Ag-site doping and Nb-site vacancies on the energy storage properties of $AgNbO_3$-based antiferroelectric ceramics remains unknown. Therefore, in this work, Ag was replaced with Nd, the Ta content was maintained at 20 mol.%, and Nb-site vacancies were produced to compensate for the valence imbalance. $Ag_{1-x}Nd_xNb_{0.8-0.4x}Ta_{0.2}O_3$ (ANNx, x = 1, 2 and 3 mol.%), ceramics were prepared using solid state reaction method.

2. Experimental Work

$AgNbO_3$ (AN) and $Ag_{1-x}Nd_xNb_{0.8-0.4x}Ta_{0.2}O_3$ (x = 1, 2 and 3 mol.%), abbreviated as ANNx ceramics were fabricated by a solid-state reaction, involving Ag_2O (>99%, Acros Organics), Nd_2O_3 (>99.9%, Sigma-Aldrich), Nb_2O_5 (>99.9%, Sigma-Aldrich) and Ta_2O_5 (>99.9%, Sigma-Aldrich) raw chemicals. Stoichiometric weighed quantities of dried raw powders were ball-milled for 6 h. The powders were then dried, calcined for 6 h at 900°C in oxygen, then ball-milled for another 6 h. The dried powders were compressed uniaxially into 8 mm-diameter pellets, which were subsequently sintered for 4 h at 1100–1150°C in oxygen.

A Bruker D2 phaser benchtop system was used to conduct X-ray diffraction (XRD) on ceramic powders. The surface morphology of polished and thermally etched materials was studied using a FEI Inspect F50 scanning electron microscope (SEM) with a backscattered electron (BSE) and an energy dispersive X-ray spectroscopy (EDS) detector. Twenty minutes of thermal etching was conducted at 90% of the sintering temperature. Using an Agilent 4184A precision LCR meter, frequency and temperature-dependent permittivity and dielectric loss were measured from ambient temperature to 500°C on pellets with coated gold electrodes on opposing parallel sides. Impedance spectroscopy (IS) data were collected from 20 Hz to 2 MHz using an Agilent E4980A analyzer. ZView software (Scribner Associates, Inc.) was used to perform a geometric correction on the IS data (area/thickness, cm). The ferroelectric test system (PolyK Technologies, PA, USA) was used to measure polarization-electric field (P-E) loops.

3. Results and Discussion

The XRD patterns of the AN and ANNx ceramics are shown in Fig. 1(a). Even with the introduction of Nb-site vacancies, all XRD diffraction peaks can be reliably assigned to single-phase perovskite structures, demonstrating that Nd and Ta co-doping will work effectively to form solid solutions. To facilitate the comparisons, the peak-related crystal planes are indexed in a cubic configuration in Fig. 1(a). Lattice parameters are extracted using the Rietveld refinement based on the *Pbcm* symmetry and are presented in Fig. 1(b). The lattice parameters a, b and c all decrease as Nd content rises, whereas c rises in comparison to AN and ANN1. However, as seen in Fig. 1(c), the overall cell volume decreases as the Nd concentration increases, which is consistent with the shift of (110) peaks to the higher 2θ angle as shown in the enlarged image in Fig. 1(a). According to Shannon's radii, the ionic radius of Nd^{3+} in 12-fold coordination is 1.27 Å, which is less than Ag^+ (1.48 Å)[36] and Ta^{5+} has a lower electronegativity than Nb^{5+} despite having the same ionic radius.[31] Therefore, replacing Ag^+ with Nd^{3+} and Nb^{5+} with Ta^{5+} may cause a reduction in cell volume, regardless of the presence or absence of A-site and B-site vacancies. This is almost consistent with the reported studies on A-site lanthanide doping in AN.[20,21,27,28]

Figure 2 shows the BSE images of thermal etched samples. Dense ceramic samples with compacted microstructure are obtained. All samples show no secondary phases or noticeable defects. The average grain size drops from 6 to 3 μm as Nd concentration increases, combined with a little increase in porosity, demonstrating that Nd doping can resist grain growth. This could be due to the fact that increasing the Nd content makes the ceramic sample more refractory and has a much higher sintering temperature. The EDS mapping images of ANN3 demonstrate the uniform distribution of elements in the ceramic samples.

Figure 3 illustrates the temperature dependence of permittivity and dielectric loss of AN and ANNx ceramics across

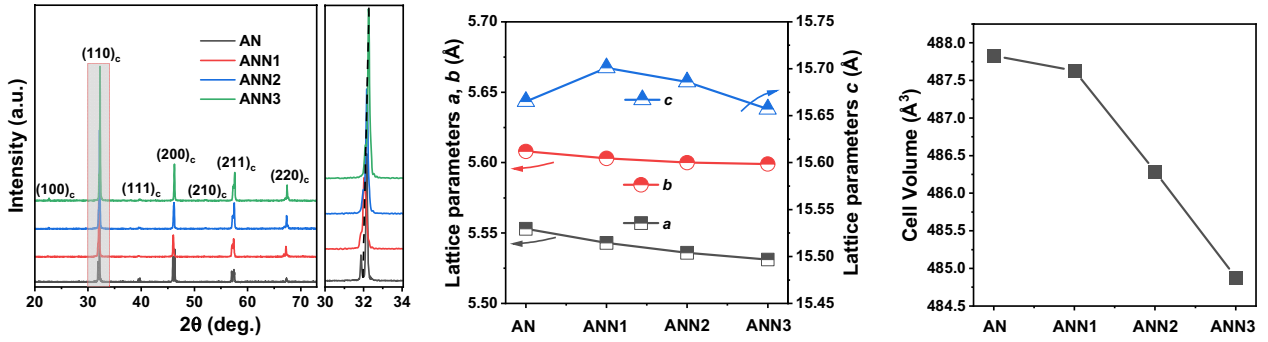

(a) (b) (c)

Fig. 1. (a) XRD patterns and an enlarged view in the range of 30–34°, (b) lattice parameters and (c) cell volume for AN and ANNx ceramics.

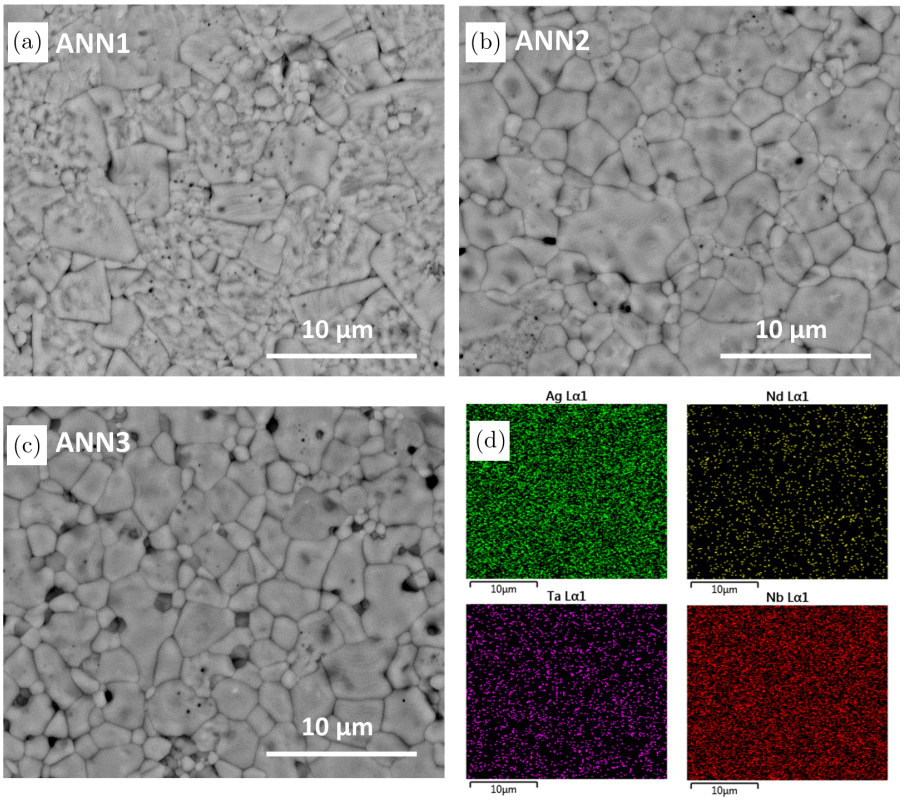

Fig. 2. BSE images of thermal etched ANN*x* ceramics (a) ANN1, (b) ANN2, (c) ANN3 and (d) EDS mapping images of ANN3 ceramic.

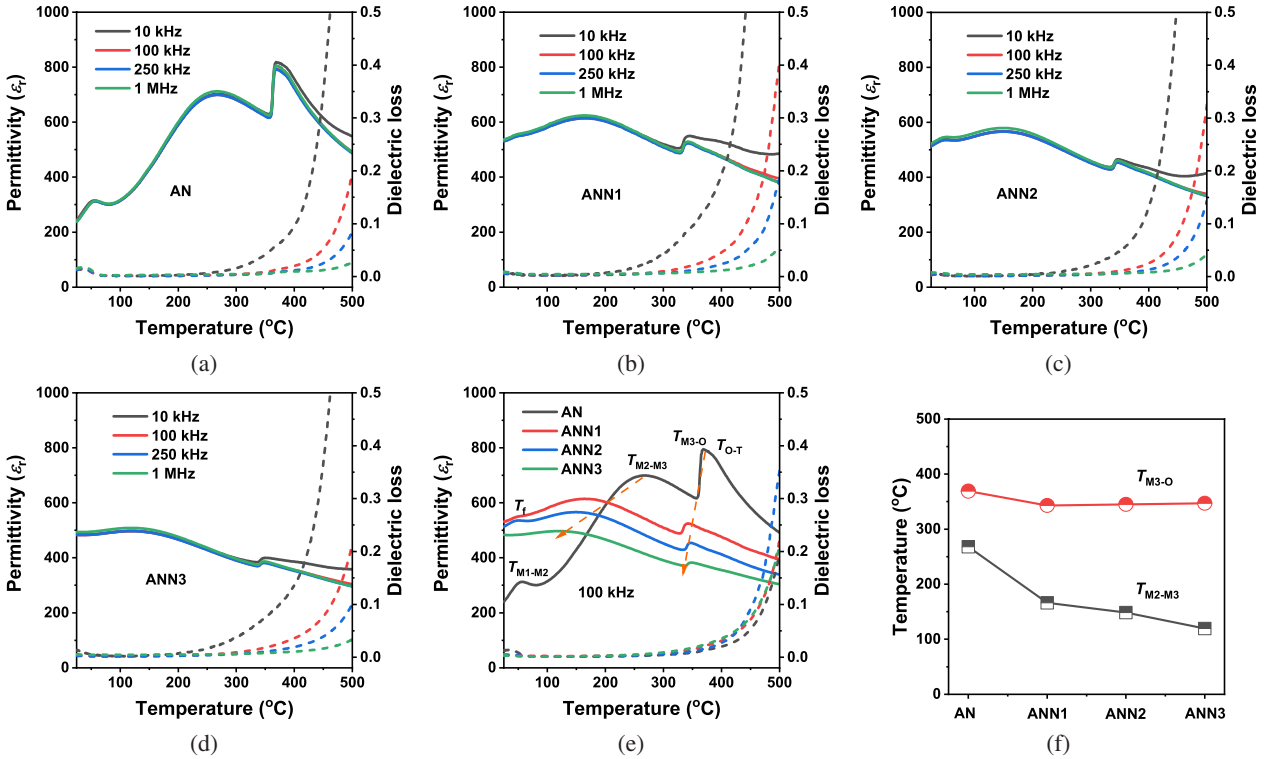

Fig. 3. Temperature dependence of permittivity and dielectric loss of (a) AN, (b) ANN1, (c) ANN2, (d) ANN3 and (e) AN and ANN*x* ceramics at 100 kHz. (f) Phase transition temperatures for the AN and ANN*x* ceramics.

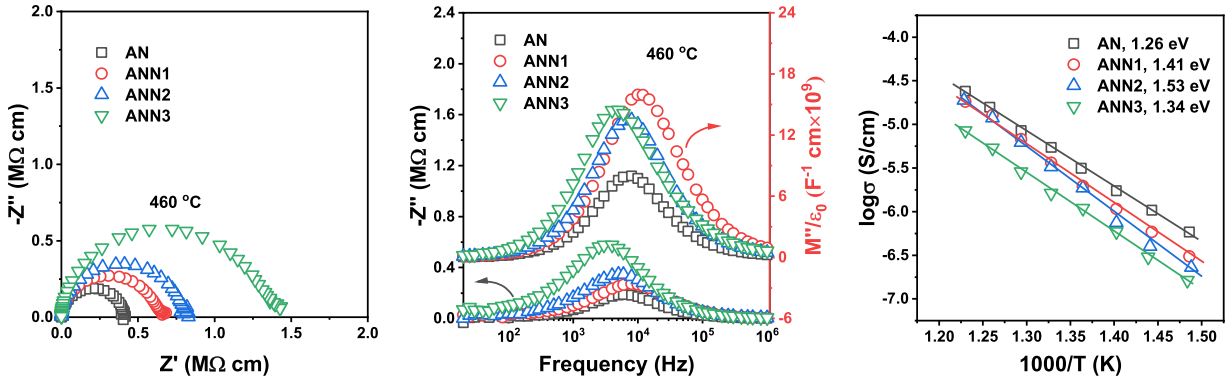

Fig. 4. (a) Z^* plots at 460°C, (b) Z'' and M'' spectroscopic plots at 460°C and (c) the Arrhenius plots of electrical conductivity extracted from M'' spectroscopic plots for the AN and ANNx ceramics.

the frequency range of 10 kHz–1 MHz. Four dielectric anomalies are connected to a series of phase transitions (M1–M2, M2–M3, M3–O and O–T) in the pure AN ceramic as shown in Fig. 3(a), which is consistent with the reported data.[37,38] For AN, the temperatures of the M1–M2 and M2–M3 phase transitions are around 67°C and 267°C, respectively. High-temperature phase transitions at 353°C and 387°C are associated with the M3–O and O–T phase transitions, respectively.[17] Comparing AN to ANN1 in Fig. 3(e), the phase transition temperatures $T_{M1–M2}$, $T_{M2–M3}$ and $T_{M3–O}$ shift to temperatures below room temperature, falling by about 100°C and 30°C, respectively. O–T phase transitions can hardly be observed in ANNx ceramics. As Nd concentration increases, $T_{M2–M3}$ continues to decrease while $T_{M3–O}$ increases slightly.

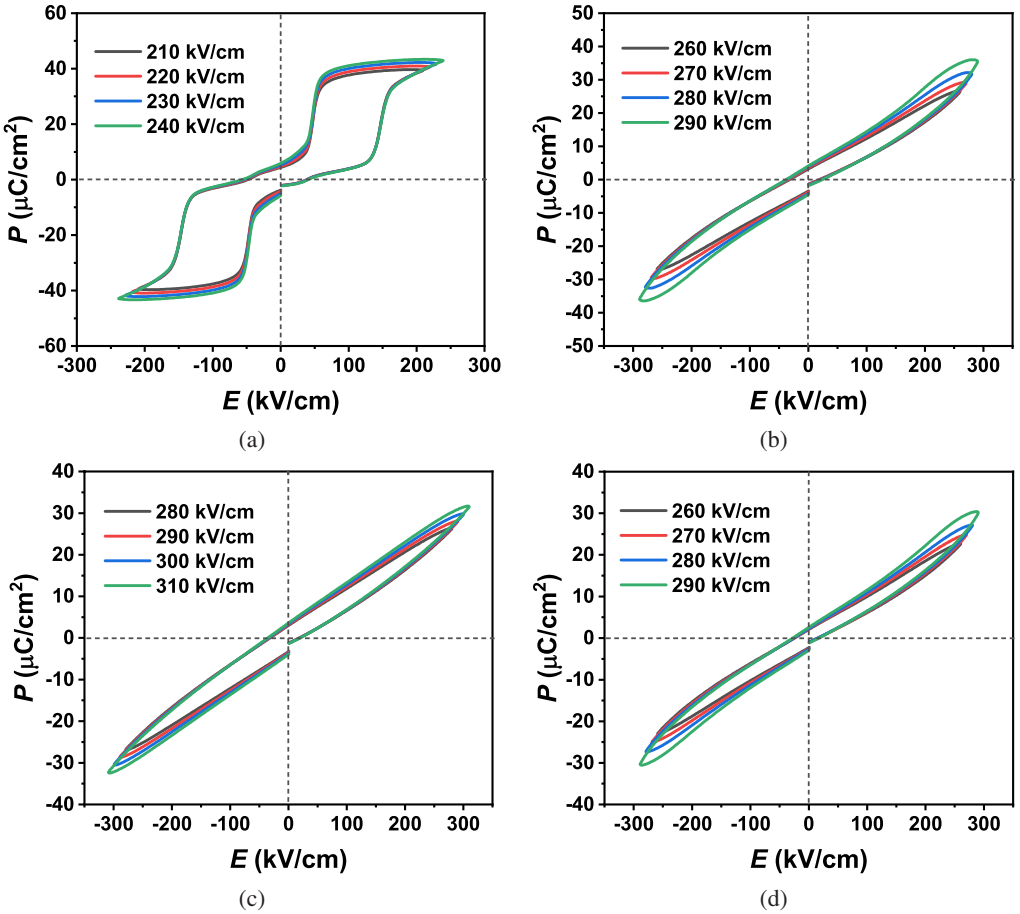

Fig. 5. *P-E* loops of (a) AN, (b) ANN1, (c) ANN2 and (d) ANN3 ceramics under various electric fields.

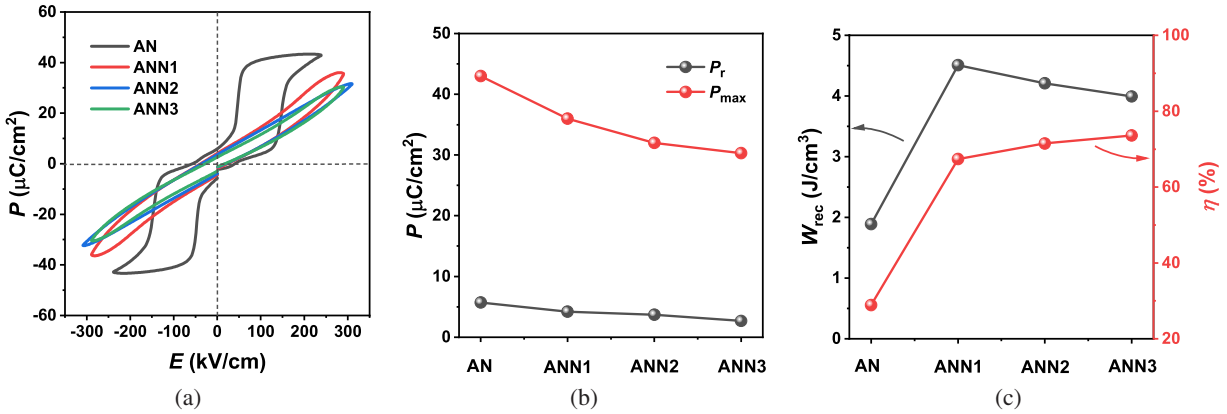

Fig. 6. Compositional variation of antiferroelectric properties at E_b (a) *P-E* loops, (b) P_{max} and P_r and (c) W_{rec} and η.

The varying trend of phase transition temperature is consistent with our prior study on Nd-doped AN,[34] proving that the presence of Nb-site vacancies does not substantially impact its trend. This may also be because there are insufficient Nb-site vacancies to trigger a dramatic change. The anomalies around 45°C for ANN1 and ANN2 have been identified as the freezing temperature (T_f), at which antipolar dipoles freeze.[32] Importantly, both the $T_{M1–M2}$ and T_f for ANN3 drop below room temperature. This suggests that the antiferroelectric phase is much more stable at room temperature. In addition, the dielectric loss stays below 500°C, demonstrating that all samples have low electrical conductivity, which contributes to the high E_b.

Figure 4 displays *Z** plots, combined Z''/M'' spectroscopic plots, and Arrhenius plots for AN and ANN*x* ceramics. In the IS data, Z'' is the imaginary part of *Z** and M'' was calculated using the equation $M'' = 2\pi f\varepsilon_0 Z'$ (*f* is the frequency in Hz, $\varepsilon_0 = 8.854 \times 10^{-14}$ F/cm, and Z' is the real part of *Z**). All samples are electrically homogeneous with only one parallel RC element (bulk-type behavior), as evidenced by the presence of a typical semicircle in the *Z** plot and the appearance of a Debye peak at the same frequency in the Z'' and M'' spectroscopic plots.[10,34] The electrical conductivity (σ) of the ceramics can be computed using the equation $2\pi f_{max}RC = 1$ (where $\sigma = 1/R$ and $C = 0.5\varepsilon_0/M''$) from their M'' Debye peak positions. In Fig. 4(c), the σ decreases with Nd content. Previous research on AN has shown that the band gap is ~2.8 eV.[39] Based on the activation energy (E_a) values after doping, the electrical conduction in ANN*x* ceramics is close to intrinsic electronic conduction, where $E_g \sim 2E_a$. Notably, the E_a of ANN*x* ceramics increases first and then decreases with the continuous addition of Nd, and the E_a of ANN3 (1.34 eV) is lower than that of ANN2 (1.53 eV), which may be because too many Nb-site vacancies might reduce the band gap of ANN*x* ceramics.

In Fig. 5, AN and ANN*x* ceramics show double-like *P-E* loops, confirming the presence of the antiferroelectric characteristic. The noticeable enhancement in the phase transition field illustrates that both Nd and Ta doping improve the stability of antiferroelectric phase. The *P-E* loops progressively become slimmer as the Nd doping level rises, which corresponds to a slight gain in η.

In Fig. 6(a), the *P-E* loops at E_b for each composition are displayed. P_{max} and P_r decrease with increasing Nd concentration in ANN*x* ceramics, as shown in Fig. 6(b), indicating a more stable antiferroelectric phase. For the ANN1 ceramic, a high applied electric field of 290 kV/cm is achieved, leading to a high W_{rec} of 4.51 J/cm^3. The high W_{rec} of ANN1 ceramic is likely the result of a combination of a huge applied electric field and relatively high P_{max} and low P_r. The relationship between E_b and Nd concentration is consistent with IS data. It is worth noting that other than E_a and electrical conductivity, there are several elements that may affect E_b, including density, core-shell structure and grain size.[1] ANN2 has the greatest E_b of 310 kV/cm, as well as the highest E_a and lowest electrical conductivity. However, the drop in P_{max} of the ANN2 ceramic led to a slightly lower W_{rec} of 4.21 J/cm^3.

4. Conclusions

Antiferroelectric dense ANN*x* ceramics have been successfully produced using the solid-state reaction method. Co-doping Nd and Ta with Nb-site vacancies in AN ceramic decreases the cell volume. The average grain size and σ decrease as Nd concentration increases. Due to the low-electrical conductivity and enhanced stability of the antiferroelectric phase, ANN1 ceramics produces a high W_{rec} of 4.51 J/cm^3 at an applied electric field of 290 kV/cm. Although the percentage contribution of such a tiny number of Nb-site vacancies to the energy storage characteristics is difficult to quantify, aliovalent doping in Ag-site with Nb-site vacancies is a beneficial strategy to improve the energy storage of AN-based ceramics.

Acknowledgment

This work was supported by the Royal Society Research Grant (RGSR1221252).

References

[1]G. Wang, Z. Lu, Y. Li, L. Li, H. Ji, A. Feteira, D. Zhou, D. Wang, S. Zhang and I. M. Reaney, Electroceramics for high-energy density capacitors: Current status and future perspectives, *Chem. Rev*. **121**, 6124 (2021).

[2]L. Yang, X. Kong, F. Li, H. Hao, Z. Cheng, H. Liu, J.-F. Li and S. Zhang, Perovskite lead-free dielectrics for energy storage applications, *Prog. Mater. Sci*. **102**, 72 (2019).

[3]X. Hao, A review on the dielectric materials for high energy-storage application, *J. Adv. Dielectr*. **3**, 1330001 (2013).

[4]A. Khesro, F. A. Khan, R. Muhammad, A. Ali, M. Khan and D. Wang, Energy storage performance of Nd^{3+}-doped $BiFeO_3$–$BaTiO_3$-based lead-free ceramics, *Ceram. Int*. **48**, 29938 (2022).

[5]B. Zhang, X.-M. Chen, W.-W. Wu, A. Khesro, P. Liu, M. Mao, K. Song, R. Sun and D. Wang, Outstanding discharge energy density and efficiency of the bilayer nanocomposite films with $BaTiO_3$-dispersed PVDF polymer and polyetherimide layer, *Chem. Eng. J*. **446**, 136926 (2022).

[6]S. Zhou, Y. Pu, X. Zhang, Y. Shi, Z. Gao, Y. Feng, G. Shen, X. Wang and D. Wang, High energy density, temperature stable lead-free ceramics by introducing high entropy perovskite oxide, *Chem. Eng. J*. **427**, 131684 (2022).

[7] D. Han, C. Wang, Z. Zeng, X. Wei, P. Wang, Q. Liu, D. Wang and F. Meng, Ultrahigh energy efficiency of $(1-x)Ba_{0.85}Ca_{0.15}Zr_{0.1}Ti_{0.9}O_3$-$xBi(Mg_{0.5}Sn_{0.5})O_3$ lead-free ceramics, *J. Alloys Compd*. **902**, 163721 (2022).

[8]S. Zhou, Y. Pu, X. Zhao, T. Ouyang, J. Ji, Q. Zhang, C. Zhang, S. Sun, R. Sun, J. Li and D. Wang, Dielectric temperature stability and energy storage performance of NBT-based ceramics by introducing high-entropy oxide, *J. Am. Ceram. Soc*. **105**, 4796 (2022).

[9]X. Wang, Y. Fan, Z. Bin, A. Mostaed, L. Li, A. Feteira, D. Wang, D. C. Sinclair, G. Wang and I. M. Reaney, High discharge energy density in novel $K_{1/2}Bi_{1/2}TiO_3$-$BiFeO_3$ based relaxor ferroelectrics, *J. Eur. Ceram. Soc*. **42**, 7381 (2022).

[10]Z. Lu, G. Wang, W. Bao, J. Li, L. Li, A. Mostaed, H. Yang, H. Ji, D. Li, A. Feteira, F. Xu, D. C. Sinclair, D. Wang, S.-Y. Liu and I. M. Reaney, Superior energy density through tailored dopant strategies in multilayer ceramic capacitors, *Energy Environ. Sci*. **13**, 2938 (2020).

[11]H. Yang, Z. Lu, L. Li, W. Bao, H. Ji, J. Li, A. Feteira, F. Xu, Y. Zhang, H. Sun, Z. Huang, W. Lou, K. Song, S. Sun, G. Wang, D. Wang and I. M. Reaney, Novel $BaTiO_3$-based, Ag/Pd-compatible lead-free relaxors with superior energy storage performance, *ACS Appl. Mater. Interfaces* **12**, 43942 (2020).

[12]H. Ji, D. Wang, W. Bao, Z. Lu, G. Wang, H. Yang, A. Mostaed, L. Li, A. Feteira, S. Sun, F. Xu, D. Li, C.-J. Ma, S.-Y. Liu and I. M. Reaney, Ultrahigh energy density in short-range tilted NBT-based lead-free multilayer ceramic capacitors by nanodomain percolation, *Energy Storage Mater*. **38**, 113 (2021).

[13]H. Wang, Y. Liu, T. Yang and S. Zhang, *Adv. Funct. Mater*. **29**, 1807321 (2019).

[14]Y. Chen, J. Chen, S. Yang, Y. Li, X. Gao, M. Zeng, Z. Fan, X. Gao, X. Lu and J. Liu, A bi-functional ferroelectric $Pb(Zr_{0.52}Ti_{0.48})O_3$ films: Energy storage properties and ferroelectric photovoltaic effects, *Mater. Res. Bull*. **107**, 456 (2018).

[15]X. Liu, Y. Li and X. Hao, Ultra-high energy-storage density and fast discharge speed of $(Pb_{0.98-x}La_{0.02}Sr_x)(Zr_{0.9}Sn_{0.1})_{0.995}O_3$ antiferroelectric ceramics prepared via the tape-casting method, *J. Mater. Chem. A* **7**, 11858 (2019).

[16]Y. Tian, L. Jin, H. Zhang, Z. Xu, X. Wei, E. D. Politova, S. Y. Stefanovich, N. V. Tarakina, I. Abrahams and H. Yan, High energy density in silver niobate ceramics, *J. Mater. Chem. A* **4**, 17279 (2016).

[17]D. Yang, J. Gao, L. Shu, Y.-X. Liu, J. Yu, Y. Zhang, X. Wang, B.-P. Zhang and J.-F. Li, Lead-free antiferroelectric niobates $AgNbO_3$ and $NaNbO_3$ for energy storage applications, *J. Mater. Chem. A* **8**, 23724 (2020).

[18]L. Zhao, J. Gao, Q. Liu, S. Zhang and J. F. Li, Silver niobate lead-free antiferroelectric ceramics: Enhancing energy storage density by B-site doping, *ACS Appl. Mater. Interfaces* **10**, 819 (2018).

[19]L. Zhao, Q. Liu, S. Zhang and J.-F. Li, Lead-free $AgNbO_3$ anti-ferroelectric ceramics with an enhanced energy storage performance using MnO_2 modification, *J. Mater. Chem. C* **4**, 8380 (2016).

[20]J. Gao, Q. Liu, J. Dong, X. Wang, S. Zhang and J. F. Li, Local structure heterogeneity in Sm-doped $AgNbO_3$ for improved energy-storage performance, *ACS Appl. Mater. Interfaces* **12**, 6097 (2020).

[21]N. Luo, K. Han, F. Zhuo, C. Xu, G. Zhang, L. Liu, X. Chen, C. Hu, H. Zhou and Y. Wei, Aliovalent A-site engineered $AgNbO_3$ lead-free antiferroelectric ceramics toward superior energy storage density, *J. Mater. Chem. A* **7**, 14118 (2019).

[22]N. Luo, K. Han, F. Zhuo, L. Liu, X. Chen, B. Peng, X. Wang, Q. Feng and Y. Wei, Design for high energy storage density and temperature-insensitive lead-free antiferroelectric ceramics, *J. Mater. Chem. C* **7**, 4999 (2019).

[23]N. Luo, K. Han, L. Liu, B. Peng, X. Wang, C. Hu, H. Zhou, Q. Feng, X. Chen and Y. Wei, Lead-free $Ag_{1-3x}La_xNbO_3$ antiferroelectric ceramics with high-energy storage density and efficiency, *J. Am. Ceram. Soc*. **102**, 4640 (2019).

[24]K. Han, N. Luo, S. Mao, F. Zhuo, L. Liu, B. Peng, X. Chen, C. Hu, H. Zhou and Y. Wei, Ultrahigh energy-storage density in A-/B-site co-doped $AgNbO_3$ lead-free antiferroelectric ceramics: Insight into the origin of antiferroelectricity, *J. Mater. Chem. A* **7**, 26293 (2019).

[25]K. Han, N. Luo, S. Mao, F. Zhuo, X. Chen, L. Liu, C. Hu, H. Zhou, X. Wang and Y. Wei, Realizing high low-electric-field energy storage performance in $AgNbO_3$ ceramics by introducing relaxor behaviour, *J. Materiomics* **5**, 597 (2019).

[26]K. Han, N. Luo, Y. Jing, X. Wang, B. Peng, L. Liu, C. Hu, H. Zhou, Y. Wei, X. Chen and Q. Feng, Structure and energy storage performance of Ba-modified $AgNbO_3$ lead-free antiferroelectric ceramics, *Ceram. Int*. **45**, 5559 (2019).

[27]J. Gao, Y. Zhang, L. Zhao, K.-Y. Lee, Q. Liu, A. Studer, M. Hinterstein, S. Zhang and J.-F. Li, Enhanced antiferroelectric phase stability in La-doped $AgNbO_3$: Perspectives from the microstructure to energy storage properties, *J. Mater. Chem. A* **7**, 2225 (2019).

[28]C. Xu, Z. Fu, Z. Liu, L. Wang, S. Yan, X. Chen, F. Cao, X. Dong and G. Wang, La/Mn codoped $AgNbO_3$ lead-free antiferroelectric ceramics with large energy density and power density, *ACS Sustain. Chem. Eng*. **6**, 16151 (2018).

[29]Y. Tian, L. Jin, H. Zhang, Z. Xu, X. Wei, G. Viola, I. Abrahams and H. Yan, Phase transitions in bismuth-modified silver niobate ceramics for high power energy storage, *J. Mater. Chem. A* **5**, 17525 (2017).

[30]Z. Yan, D. Zhang, X. Zhou, H. Qi, H. Luo, K. Zhou, I. Abrahams and H. Yan, Silver niobate based lead-free ceramics with high energy storage density, *J. Mater. Chem. A* **7**, 10702 (2019).

[31]L. Zhao, Q. Liu, J. Gao, S. Zhang and J. F. Li, Lead-free antiferroelectric silver niobate tantalate with high energy storage performance, *Adv. Mater*. **29**, 1701824 (2017).

[32]Y. Tian, L. Jin, Q. Hu, K. Yu, Y. Zhuang, G. Viola, I. Abrahams, Z. Xu, X. Wei and H. Yan, Phase transitions in tantalum-modified silver niobate ceramics for high power energy storage, *J. Mater. Chem. A* **7**, 834 (2019).

[33]N. Luo, K. Han, M. J. Cabral, X. Liao, S. Zhang, C. Liao, G. Zhang, X. Chen, Q. Feng, J. F. Li and Y. Wei, Constructing phase boundary in $AgNbO_3$ antiferroelectrics: Pathway simultaneously achieving high energy density and efficiency, *Nat. Commun*. **11**, 4824 (2020).

[34]Z. Lu, W. Bao, G. Wang, S.-K. Sun, L. Li, J. Li, H. Yang, H. Ji, A. Feteira, D. Li, F. Xu, A.K. Kleppe, D. Wang, S.-Y. Liu and I. M. Reaney, Mechanism of enhanced energy storage density in $AgNbO_3$-based lead-free antiferroelectrics, *Nano Energy* **79**, 105423 (2021).

[35]S. Li, H. Nie, G. Wang, C. Xu, N. Liu, M. Zhou, F. Cao and X. Dong, Significantly enhanced energy storage performance of rare-earth-modified silver niobate lead-free antiferroelectric ceramics via local chemical pressure tailoring, *J. Mater. Chem. C* **7**, 1551 (2019).

[36]R. D. Shannon, Revised effective ionic radii and systematic studies of interatomic distances in halides and chalcogenides, *Acta Crystallogr. A* **32**, 751 (1976).

[37]I. Levin, J. C. Woicik, A. Llobet, M. G. Tucker, V. Krayzman, J. Pokorny and I. M. Reaney, Displacive ordering transitions in perovskite-like $AgNb_{1/2}Ta_{1/2}O_3$, *Chem. Mater*. **22**, 4987 (2010).

[38]K. Y. Yasuhiro Yoneda and S. Kohara, Structural investigations of $AgNbO_3$ phases using high-energy X-ray diffraction, *Trans. Mater. Res. Soc. Jpn*. **37**, 73 (2012).

[39]H. K. Hideki Kato and A. Kudo, Role of Ag^+ in the band structures and photocatalytic properties of $AgMO_3$ (M Ta and Nb) with the perovskite structure, *J. Phys. Chem. B* **106**, 12441 (2002).